RSC Advances

PAPER

View Article Online
View Journal | View Issue

Cite this: *RSC Adv.*, 2024, **14**, 1563

Design and fabrication of a polydimethylsiloxane device for evaluating the effect of pillar geometry and configuration in the flow separation using deterministic lateral displacement†

Pavan Pandit, [ab] Lingxue Kong [b] and G. L. Samuel *[a]

The advancement of microfluidics and the manufacturing of microdevices has led to a strategic change in the biomedical industry. The flow through narrow channels and the pillars are placed strategically, leading to the phenomenon of particle separation through deterministic lateral displacement (DLD). In such a phenomenon, the shape, size, location and orientation of the obstacles play an important role. For the first time, particle separation is achieved with DLD modules having high row shift angles of 25°, 30° and 35°, reducing the number of pillars. The significance of circular and triangular micropillars executing deterministic lateral displacement, oriented at different angles, has been investigated, and it is found that the triangular pillars oriented at 75° resulted in better separation compared to the other configurations. In this report, the fabrication, location, orientation of the micropillars and the selection of appropriate process parameters are detailed. The structures are fabricated on silicon wafers using the standard photolithography process followed by the deep reactive ion etching process. These dies are further used to fabricate the polydimethylsiloxane-based microfluidic chips. These fabricated devices are characterised by their size, structure and quality using 3D microscopy and scanning electron microscopy. Further, blood plasma separation is carried out using the devices fabricated in this work, and the particles at the inlet and outlets are evaluated using microscopy and a novel image processing technique, replacing the use of a hemocytometer. The path traced by the particles at different flow conditions is numerically evaluated and validated with experiments. The novel device is capable of separating blood cells from plasma with a recovery factor varying from 44% to 100%. PDMS–PDMS bonding experiments using oxygen and argon plasma have been carried out to evaluate the maximum bond strength and flow velocity in the devices. It is observed that the oxygen plasma results in a bond strength of 0.404 N mm^{-1}, thus a high throughput of 135.34 μL s^{-1} is achieved using the fabricated device.

Received 21st September 2023
Accepted 20th November 2023

DOI: 10.1039/d3ra06431j

rsc.li/rsc-advances

1 Introduction

Particle separation in fluids is carried out using various methods, prominently using centrifugation, chromatography and other size-based methods. These conventional particle separation techniques are either slow or discrete. Discrete and slow particle separation is undesirable in therapeutics, dialysis, and blood purification applications. Rapid separation is an essential feature in continuous purification as it defines the efficiency of the system. Continuous separation of particles in fluid flow is carried out using active and passive separation techniques. Particle separation can be based on size, shape, density, mass, and electric and magnetic properties.[1–3]

Continuous rapid separation of cells is crucial in the case of blood purification. The process has to be carried out so that it does not affect the functionality of the blood cells. If the process or system induces pressure gradients, biotoxicity, ionic imbalance or change in the flow behaviour, the blood gets coagulated or is rendered unusable. Hence, special care has to be taken while designing these systems. The material used in the fabrication of these devices is essentially biocompatible. The fabrication techniques should not induce biotoxicity such as corrosion, zincification or other chemical reactions. The design of the systems is such that the pressure gradients induced are minimal such that the function of the system is not compromised.

Considering these features, various systems have been established. The deterministic lateral displacement technique

[a]*Manufacturing Engineering Section, Department of Mechanical Engineering, IIT Madras, Chennai, Tamil Nadu, 600036, India. E-mail: samuelgl@iitm.ac.in*

[b]*Institute for Frontier Materials, Deakin University, Geelong, Victoria, 3216, Australia*

† Electronic supplementary information (ESI) available. See DOI: https://doi.org/10.1039/d3ra06431j

is one such type of continuous separation technique. DLD has been used in the applications such as emulsifying droplets in water-in-oil or oil-in-water systems,[4] encapsulation of micro-organisms,[5] separation of biological particles like DNA,[6,7] exosomes,[8,9] blood cells,[10–14] mammalian cells and circulating tumour cells.[15,16] It was first demonstrated by Huang *et al.*[7] using micropillars with a circular cross-section, primarily used for rapid DNA separation. The DLD was further improved by Inglis[17] and Davis[14] and considering the wall effect and the parabolic velocity profile in the inter-pillar spaces. Furthermore, by changing the profile, shape and dimensions of the micropillars and the microchannels, the critical diameter of the particles being separated varies. The pillars with circular, triangular, rhomboidal and octagonal cross sections have been analysed previously. The pillars with unconventional cross-sections like streamlined, airfoil,[18] and I-section[19,20] were analysed to reduce the critical diameter of the separating particles. Loutherback *et al.*,[21,22] showed that the triangular posts aided in reducing the critical diameter of the separating particles by considering various factors such as the gap-to-post size, the vertex rounding, and the width-to-height ratio of the triangle. It is seen that the pillars with a cross-section of an equilateral shape performed better, considering the critical size of the particles. Improving the Davis model, Wei *et al.*[23] developed a numerical model to study the lateral displacement of spherical particles using the lattice Boltzmann method and immersed boundary approach. This model predicts the particle path and the critical particle diameter in DLD systems with shaped pillars. Dincau *et al.*[18] proposed the effect of Reynolds number on the particle path. In the study, it was observed that the streamlines of the flow at different Re differed in their positions. Further, Pariset *et al.*[24] studied the effect of the number of pillars in the channel width (w_c) and anticipated the minimum number required to avoid the intermediary mode. The study also demonstrates the existence of multiple critical diameters and the techniques to obtain a single critical diameter in the entire regime.

Solid polymeric microspheres are used abundantly in the flow characterisation of the devices, but the blood components are soft and deformable.[25] It is seen that the behaviour of the particles also depends on the shape of the particles being separated.[20] Patel and Stark[26] conducted on the spherical and biconcave particles in various clustering configurations, such as monodispersed and bi-dispersed pairs. Thus, in this study, whole blood is considered for the analysis. The blood contains erythrocytes, leukocytes[27] and thrombocytes, mostly biconcave in shape.

These DLD structures and the microchannels are fabricated by various processes such as lithography and lift-off processes, electroplating, thermal oxidation, wire bonding, chemical etching, deep reactive ion etching, and laser micromachining. The most prominent technique used in the fabrication through photolithography is SU-8 lithography. However, cracking and residual stresses[28] were observed in the SU-8 lithography affecting the quality of the DLD module. The other challenges associated with the above-mentioned process are that the cross-section of the slender pillars is non-uniform owing to the non-isotropic etching, the heat-affected zone, and the fusion of the adjacent micro holes. In our previous study, the P20 die steel moulds were prepared using femtosecond lasers to fabricate PDMS-based microchannels with DLD structures.[29] Thus, the current structures are fabricated considering the limitations of laser micromachining in fabricating the DLD structures.

Bonding of the microfluidic chips is crucial in determining the throughput of the device. It defines the maximum flow rate of the fluid. Various bonding techniques are adopted to bind the PDMS–PDMS chips. Some prominent techniques are partial curing, adhesive bonding, solvent bonding and plasma bonding techniques. The binding of the PDMS chips occurs due to the creation of hydroxyl (–OH) groups on the surface when PDMS is exposed to oxygen plasma. The –OH groups readily react to form covalent bonds with the other plasma-exposed PDMS chip.[30] The bond strength is quantified using blister, leakproof, and adhesion tests. It was observed that the bond strength of O_2 and argon (Ar) plasma treat PDMS samples showed similar bond strengths when PDMS was bonded with glass coverslips.[31]

In this study, micropillars with circular and equilateral triangular cross-sections are considered to evaluate the effect of the process parameters, vertex rounding, placement and the orientation of the pillars in the deterministic lateral displacement zone. Numerical simulations are carried out, and validated with experiments through blood flow evaluation. The fabrication of the masters to develop the PDMS chips is explained in detail showing the variations in the pillar depth with the etching cycles. The structures are characterised by evaluating their quality and shapes. Finally, the adhesive bond strength evaluation of the PDMS–PDMS samples was carried out to determine the blood flow's maximum pressure and mass flow rate in the microchannels.

2 Materials and methods

2.1 Materials

Chromium coated quartz glass plate is used for the preparation of the mask. 4 inch ⟨100⟩ 0.5 mm uncoated N type Phos 1–10 ohm SSP silicon wafers are used in the fabrication of the masters. Photolithography is used to prepare the masters. A positive photoresist (AZ40XT) and AZ-726 MIF developer are used for the photolithography process. C_4F_8 and SF_6 gases are utilised for the Bosch process.[32] Commercially available COMSOL Multiphysics 5.6 is used to carry out the flow simulations. Human blood collected from healthy individuals at the institute hospital is used to conduct flow experiments and validate the simulation results. The experiments are carried out as per the institute guidelines with approval from the institutional Ethical Committee of the Indian Institute of Technology – Madras with protocol number IEC/2018/01/GLS/16. Informed and signed consent is obtained and archived to conduct the experiments and publish results.

2.2 Device configuration

Open source K-layout is used to design the geometry for photolithography. Fig. 1 shows the schematic layout of the

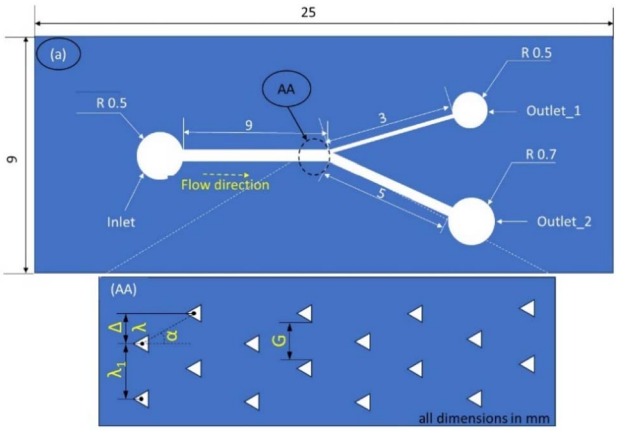

Fig. 1 The individual device with nomenclature.

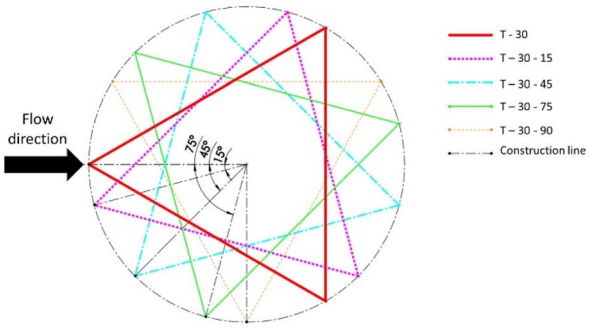

Fig. 2 Sign convention followed to determine the rotation angle with respect to the flow direction considering initial T-30 as 0°.

devices to be fabricated with 1 inlet and 2 outlets. The devices comprise of straight channels of width 500 μm and length 90 mm. Each device is provided with a different configuration of the deterministic lateral displacement structures. The configurations are detailed in Table 1.

2.3 Fabrication of PDMS devices

2.3.1 Fabrication of mask. The mask was written on SF-100 micro writer using the chromium-plated quartz glass with the configurations as summarized in Table 1. The designs used in the fabrication are provided in Fig. S1,† and the scheme of orientation of the triangular pillars is shown in Fig. 2.

2.3.2 Fabrication of masters using photolithography. Silicon wafers were used as the substrate for the fabrication of the masters. 4 inch ⟨100⟩ 0.5 mm uncoated N type Phos 1–10 ohm SSP silicon wafers were used for the fabrication. The chosen wafers were piranha cleaned using a 3 : 1 mixture of hydrogen peroxide and sulphuric acid to remove the organic residues on the silicon surface. The wafers were placed on the hot plate maintained at 120° to remove the solvent impurities. After assuring that the wafers are free from organic or any dirt, a layer of hexamethyldisilazane is spin-coated on the silicon surface.

A layer of positive photoresist, namely AZ40xt, was spin coated on the HMDS coated silicon wafers. The coated wafer is subjected to pre-exposure bake at 80° on the hot plate. The baked wafers are then exposed to UV light with the mask aligned on it. This is carried out using the UV flood light. The UV exposure required to cure the AZ40xt is 12 W cm^{-2}, *i.e.*, the wafer is exposed to UV light at 25 W for 75 s.[33] The exposed wafers are then subjected to post-exposure bake of 80 °C for 10 min. The unexposed portion of the coated wafer is removed by developing the wafer using the AZ726 MIF developed.

2.3.3 DRIE of silicon wafers. The wafers developed using photolithography are subjected to DRIE, as the process results in perpendicular walls. The system uses alternating etch (SF_6) and passivation (C_4F_8) cycles to achieve high aspect ratio structures (~1 : 10).[34] The equipment used here is the Si Oxford PlasmaLab DRIE machine. The recipe used to carry out the deep reactive ion etch is summarized in Tables 2 and 3.

According to the hypothesis, every cycle etches 385 nm of the silicon wafer. To determine the etch rate, three different

Table 2 Details of the parameters used during DRIE – Bosch etch

Parameter	Value
Chamber pressure (mTorr)	30
Passivation pressure (mTorr)	19
Valve position	70%
SF_6 flow rate (ccpm)	140
C_4F_8 flow rate (ccpm)	7
ICP generator forward power (W)	2200
RF generator forward power (W)	23
Step time (s)	6

Table 1 Details of the fabricated DLD structures configurations

Sl no.	Configuration code	Post shape	Inclination angle	Tilt angle	Row shift fraction
1	C – 25	Circular	25	—	0.4663
2	C – 30	Circular	30	—	0.5774
3	C – 35	Circular	35	—	0.7002
4	T – 25	Triangular	25	0	0.4663
5	T – 30	Triangular	30	0	0.5774
6	T – 35	Triangular	35	0	0.7002
7	T – 30–15	Triangular	30	15	0.4663
8	T – 30–45	Triangular	30	45	0.4663
9	T – 30–75	Triangular	30	75	0.4663
10	T – 30–90	Triangular	30	90	0.4663

Table 3 Details of the parameters used during deposition

Parameter	Value
Chamber pressure (mTorr)	30
Passivation pressure (mTorr)	19
Valve position	70%
SF_6 flow rate (ccpm)	4
C_4F_8 flow rate (ccpm)	140
ICP generator forward power (W)	1700
RF generator forward power (W)	4
Step time (s)	5

combinations were carried out at 256, 258 and 259 cycles and it was seen that 258 cycles yielded a channel depth of 100 μm, which was the intended dimension, as discussed in Section 3.1.2.

After the DRIE of the silicon wafer, the remaining resist was washed away with acetone. The cleaned wafer was further deposited with the passivation layer such that the Teflon-like nano-coating acts as a release agent while fabricating the PDMS devices. The fabricated silicon masters are shown in Fig. 3 and detailed figures are shown in Fig S2.†

2.3.4 Fabrication of PDMS device using spin coating. PDMS was mixed in the ratio of 10 : 1 inside a mixer with two 90 second cycles, the first being run at 1000 rpm and the second run at 500 rpm. Simultaneously, the silicon wafer is placed in a vacuum chamber for silanisation (20 μL of (3-aminopropyl) triethoxysilane is placed on a glass slide in the chamber, and the vapours are allowed to deposit on the wafers). The PDMS mix is poured on the coated wafer and then placed in a vacuum chamber until the microbubbles escape from the mould. After the degasification, the assembly is kept in a hot air chamber maintained at 65 °C for 2 h Fig. 4 shows the fabrication technique used in the development of the microfluidic device.

2.3.5 Theory of DLD. The flow in the DLD domain can be modelled using the 2D Navier–Stokes equation (eqn (1)).[7,35] The flow depends on the value of the dimensionless numbers, such as Reynolds' number given in eqn (2). This dimensionless number depends on the density, velocity, dynamic viscosity and hydraulic diameter. The hydraulic diameter for the given cross-section is given by eqn (3). In this case, the cross-sectional area of the microchannel is 5×10^{-2} mm^2, and the perimeter is 1.2 mm, resulting in a hydraulic diameter of 0.167 mm. The length of the channel considered is 30 mm. The Re is evaluated using the D_H of 0.167 mm, density of 1000 kg m^{-3}, flow velocity of 25 mm s^{-1} and a dynamic viscosity of 1×10^{-3} Pa.

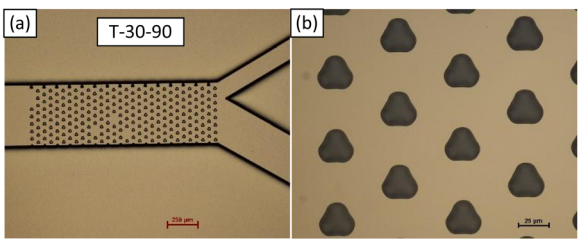

Fig. 3 Microscopic image of the device, (a) 5×, (b) 50×.

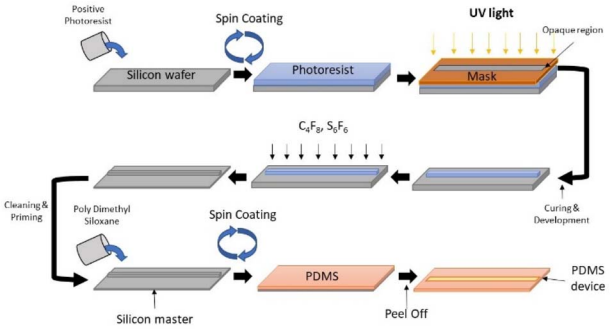

Fig. 4 Fabrication process used in developing the microfluidic device.

$$\rho\frac{\partial \bar{v}}{\partial t} + \rho(\bar{v}\nabla)\bar{v} = -\nabla p + \mu\nabla^2\bar{v} \quad (1)$$

$$\mathrm{Re} = \frac{\rho v D_H}{\gamma} \quad (2)$$

$$D_H = \frac{4 \times A_c}{P} \quad (3)$$

Due to the low Re, in other terms due to the prominence of viscous damping, the kinetic energy term in eqn (1) becomes negligible, thus can be written as eqn (4).

$$\rho\frac{\partial v}{\partial t} = -\nabla p + \mu\nabla^2 v \quad (4)$$

Considering the pressure gradient and the volumetric fluid flux between the pillars. The fluid resistance is deduced as shown in eqn (5) considering the circular pillars and the parabolic velocity profile between the pillars $\left(v_{max} = \frac{3}{2} \times v_{avg}\right)$.

$$R = \frac{12\mu L}{G^3 E} \quad (5)$$

Further, considering the allowable shear stress (0.3 Pa in large arteries and 10 Pa in capillaries) in the blood vessels, which prevents the activation of the platelets. This is observed to be maximum at the walls

$$\left(\text{Shear rate } (\dot{\gamma}) = \frac{4 \times v_{max}}{G}\right)$$

Therefore, the critical hydrodynamic diameter is twice the width of the first streamline, thus

$$D_c = 2\zeta G\varepsilon \quad (6)$$

where, ζ is a function of shape and row shift fraction of the array.

$$\text{Row shift fraction } (\varepsilon) = \frac{\int_0^{\zeta G} v_y dx}{\int_0^{G} v_y dx}$$

The row shift fraction signifies the fractional distance by which the adjacent row is shifted, and this is vital in determining the separation efficiency of the device. Analytically, the least critical diameter is found to be 19.31 μm, computed using eqn (6).

2.3.6 Bonding of the devices with substrate

2.3.6.1 Bonding of the devices with PDMS. The PDMS–PDMS bonding, which is crucial in determining the flow pressure, is tested using the 180° T-peel test (ASTM D1876).[30] The peel test is done using the micro tensile testing machine. Initially, the PDMS–PDMS bond is created using the parameters mentioned in Table 4. A bond strip of width 10 mm is cut out to carry out the experiments. A small area of the bond is broken to create the free ends of the PDMS layers. The two free ends of the PDMS are held in the jaws of the tensile testing machine as shown in Fig. S4.† The experiment was carried out at a steady extension rate of 20 mm min^{-1}. The load *vs.* extension graph of the bond is observed. The maximum load observed in the load *vs.* extension is utilised for the analysis. This determines the threshold of the fluid flow pressure since increasing the pressure beyond this limit will result in the delamination of the two PDMS layers.

2.4 Fluid flow experiments

The flow of the particles depends on the velocity of the fluid, density of the particles and the size of the particles. The flow in the microchannels provided with the DLD structures is simulated using COMSOL Multiphysics. The laminar flow and the particle tracing module are used to evaluate the velocity profiles and the number of particles being separated. The boundary conditions are shown in Fig. S5.† The flow parameters, such as the inlet velocity, the density of the particles and the size of the particles flowing in the microchannels, are varied. The path taken by the particles is noted and analysed.

2.4.1 Critical flow rate. The flow through the microfluidic device here is similar to the flow through a thin-walled cylinder. The inner diameter is the hydraulic diameter, and it is assumed that the system fails at the bonding section. The maximum allowable hoop stress in the system is substituted by the bond strength of the plasma bonding. Eqn (7) is used to calculate the allowable hydrodynamic pressure in the device, and on deducing the pressure, the maximum acceptable fluid velocity is calculated. The calculated values are tabulated in Table 5.

$$\sigma_H = \frac{\Delta p \times D_H}{t} = \text{bond strength}, \left[\text{N mm}^{-2}\right] \quad (7)$$

Table 5 Boundary conditions

Parameter	Value
Type of flow	Laminar flow
Governing equation	Navier–Stokes' equation
Inlet velocity (m s^{-1})	0.5
Domain	1, 2, 3
Domain density (kg m^{-3})	1000
Domain dynamic viscosity (Pa)	0.001
Particle density (kg m^{-3})	1055
Particle diameter (μm)	10, 15
Drag force	Governed by Stokes law
Wall condition	No slip, bounce

$$Q = \frac{8\mu L \Delta p}{\pi R^4}, \left[\text{m}^3\ \text{s}^{-1}\right] \quad (8)$$

$$\text{Mass flow rate } \dot{m} = A \times v, \left[\text{m}^3\ \text{s}^{-1}\right] \quad (9)$$

The flow experiments are conducted using the experimental setup as shown in Fig. 10a. The setup consists of a syringe pump (NE-300), a fluorescent microscope (Nikon Eclipse 80i), a Nikon DS-Ri1 camera and a computer system to analyse the images. The syringe pump is used to pump the fluid at the required mass flow rates, and the fluorescent microscope and the camera are used to capture the images and videos of the cells flowing between the pillars.

2.4.2 Separation efficiency. Human blood is collected from a healthy human in a K2 EDTA blood collection tube (Make: Levac). The blood samples are diluted with different volumes of phosphate buffer solution so as to ensure that an adequate amount of cells are present in the blood samples. This makes it easier to count the cells in the haemocytometer. Fig. 12a–f show the microscopic images of the blood collected on the haemocytometer from outlet 1, and Fig. 12g–l shows the images of the blood collected from outlet 2. The microscopic images are further processed to evaluate the cells present in the samples collected from outlet 1 and outlet 2 and are represented.

2.4.3 Image processing for cell counting. The images collected from the microscope are processed using ImageJ. This involves the conversion of the image to a 8 bit black-and-white image. Further, the background of the image is removed using the subtract background command. Once the background is removed, the threshold of the image is set such that the outline

Table 4 Process parameters used in the PDMS–PDMS bonding

Configuration					
Plasma exposure	Temperature (°C)	Pressure (mTorr)	Exposure duration (mins)	Bake temperature (°C)	Post bonding bake duration (mins)
O_2	80	436	2	80	10
O_2	80	436	5	80	10
Ar	80	455	2	80	10
Ar	80	455	5	80	10

of the cells is clearly marked. Then, using the fill holes command, the cells are filled and converted to solid entities. Using the watershed command, the fused cells, if any are separated, such that the count of the cells is appropriate. The cell counter command is used to count the cells, by choosing the range of the pixels such that the cell size is appropriately chosen. The circularity of the entities is also maintained at 80% such that the other entities apart from the cells are neglected.

3 Results

3.1 Characterization of the devices

3.1.1 Scanning electron microscopy. The masters and the PDMS devices are characterized for their dimensions and geometry. The geometry of the holes and the pillars are observed using the portable scanning electron microscopy (Make: Hitachi). From Fig. 5, it is seen that the vertices of the triangular holes are rounded and the circular geometries are polygonal in shape. The shape can be attributed to the capability of the UV flood light or the mask writer. Uniform pillars of diameter 35 ± 5 μm are fabricated with rounded edges. It is also seen that PDMS is stuck in some of the shaped holes despite the application of the primer coating. Thorough cleaning with isopropanol and a thin layer of silane overcomes the problem of sticking and prevents the distortion in the shape of the micropillars in the subsequent peel-offs.

3.1.2 3D profilometer imaging. The 3D images of the devices and the masters were procured to evaluate the depth of the holes and the height of the PDMS pillars. From Fig. 6, it is

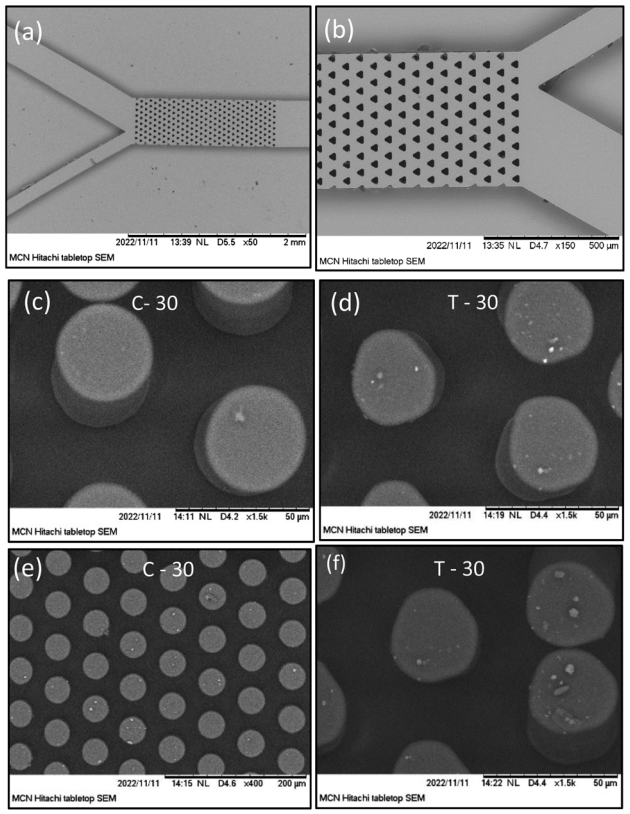

Fig. 5 Scanning electron microscopic images of the (a) and (b) silicon masters, (c)–(f) PDMS chips.

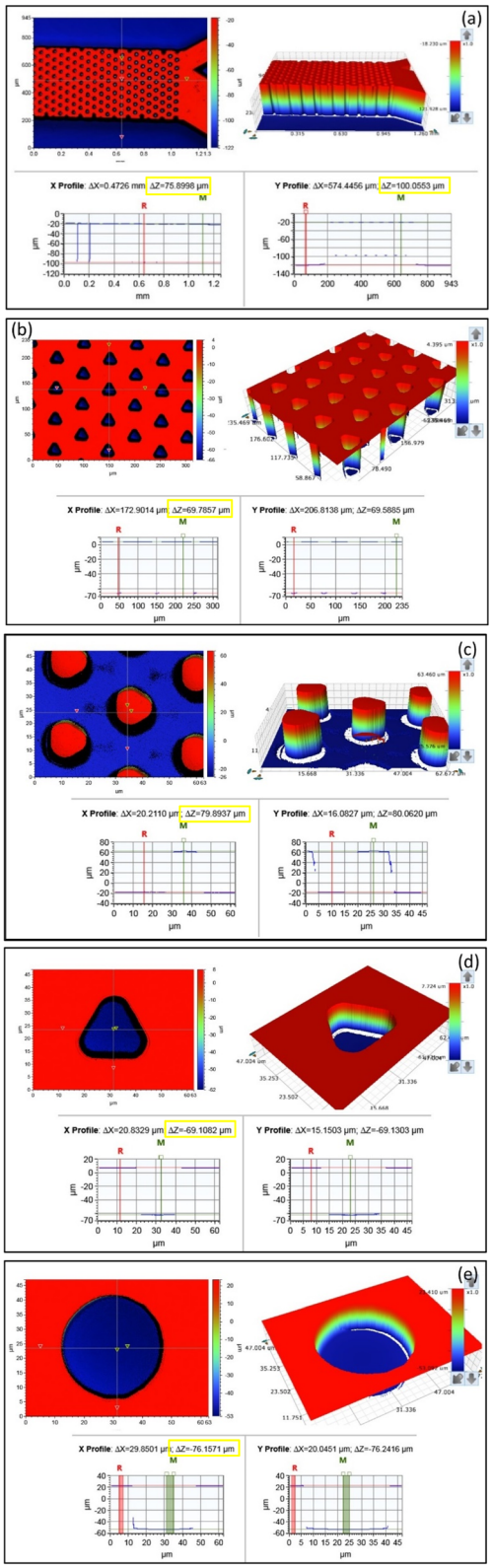

Fig. 6 3D profilometer images of the (a and b) masters and (c–e) devices, showing the channel depth, microholes and fabricated micropillars.

Table 6 Variation of depth with etch cycles

Sl no.	No. of cycles	Depth of etching (μm)	
		Channel	Hole
1	255	98.64	69.58
2	258	100.02	75.89
3	259	100.64	76.20

observed that the depth of the circular and triangular pillars was found to be 75 ± 1 μm and 69 ± 1 μm. The depth of the channel and hole varies with the etch cycles, and variation is shown in Table 6. This variation in the depths is due to the area exposed during the etch cycles.

Fig. 6a and b show the depth of the pillars and the microchannels. From the figures, it is evident that the circular and triangular pillars are 75.9 μm and 69.6 μm whereas the microchannel is 100 μm in depth. Fig. 6c shows the dimensions of the PDMS micropillars in the device. It is seen that the triangular pillars are 79.9 μm high, this variation can be attributed to the formation of defects while peeling or due to the presence of undulations on the pillar surface.

Fig. 6d and e show the variation in the depths of the micro holes of circular and triangular geometry after 255 DRIE cycles. A variation of approximately 7 μm was observed between the circular and triangular holes.

3.2 Evaluation of bond strength: peel test of the devices

Fig. 7 shows the plot corresponding to the bond strength test. The specimens 1 and 2 correspond to the chips bonded using O_2 plasma whereas the graphs corresponding to specimens 3 and 4 correspond to the chips bonded using argon plasma. The maximum load during the 180° peel test for the samples is shown in Table 7. The bond strength observed from the T-peel test is further used to evaluate the maximum fluid flow velocity and the maximum fluid flow rate. Table 8 summarises the details of the fluid flow.

3.3 Numerical simulations

With the knowledge of the maximum velocity and the flow rates, numerical simulations are carried out to observe the particle trajectories. The commercially available software tool, COMSOL Multiphysics 5.6, is used to evaluate the flow pattern and to predict the number of particles flowing in the

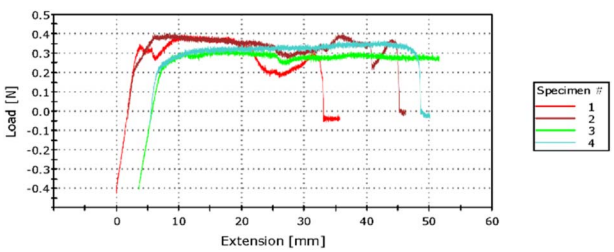

Fig. 7 The results of the T-peel test where specimen 1 and 2 corresponds to the oxygen plasma, whereas 3 and 4 to the argon plasma.

Table 7 The maximum load observed during the 180° T peel test of the O_2 and Ar bonded samples

Type of plasma	Maximum load (N)	
O_2 plasma	0.396	0.404
Ar plasma	0.322	0.366

Table 8 Flow parameters based on the simulations and bond strength

Configuration	Bond strength (N mm^{-1})	Maximum flow rate (μL s^{-1})	Maximum velocity (m s^{-1})
O_2 plasma	0.396	132.66	1.06
O_2 plasma	0.404	135.34	1.08
Ar plasma	0.366	122.61	0.98
Ar plasma	0.322	107.87	0.86

left and the right outlets. The particle tracing module in the tool helps determine the path taken by the particles. The fluid was flown at the initial velocity of 0.5 m s^{-1} and the particle size *i.e.*, the diameter was considered to be 10 μm and 15 μm. The number of particles available in each domain at 0.1 s of the simulations (refer to Fig. S3† for the results) was noted and tabulated in Table 9. From this information, the recovery factor of the device is calculated using eqn (10). It can be observed that the number of particles separated depends on the flow patterns.

It is seen that the circular pillars oriented at 35° provides the best particle separation, but as the circular pillars result in a zero velocity zone on their surface, the possibility of the particles getting stuck in the domain is higher. The recovery factor in the devices with circular pillars is lower in comparison to the devices with triangular pillars. When the particle path in the devices with triangular pillars is observed, the orientation plays an important role. The ratio of the cells in outlet 1 to the cells in outlet 2 shows an increasing trend while the orientation angle is increased from 25° to 45°, but at 75°, the ratio is the least, thus suggesting that the triangular pillars oriented at 75° show the best separation. Meanwhile, the recovery rates in case of the devices with triangular pillars is lower in comparison to the devices with circular pillars.

From Fig. 8 and 9, it is evident that the vertices of the triangular pillars also contribute to the separation efficiency of the devices. Fig. 8 shows the count of the cells observed in the 3 chosen domains considering the sharp edged micropillars whereas the Fig. 9a represents the count of the cells in the domains considering the rounded edged micropillars as in the case of the experiments. The particle size chosen for previously discussed simulations is 10 μm whereas the simulations results shown in Fig. 9b consider a particle diameter of 15 μm. Fig. 9a and b compares behaviour of the path lines when diameter is varied from 10 μm to 15 μm. It is observed that the 15 μm particles are directed towards the outlet 2 whereas the 10 μm particles have the possibility of flowing towards the outlet 1.

Table 9 The number of cells present at outlet 1 and outlet 2 suggests the separation efficiency of the devices

Configuration	Cell count in outlet 1	Cell count in outlet 2	Cell count in inlet	Cells stuck in domain 1	Ratio of out_1 to out_2
C – 25	9	10	27	7	0.90
C – 30	6	14	27	0	0.43
C – 35	0	22	27	5	0
T – 25	3	9	27	13	0.33
T – 30	6	16	27	4	0.38
T – 35	3	12	27	11	0.25
T – 30–15	4	14	27	9	0.29
T – 30–45	1	0	27	24	—
T – 30–75	2	11	27	14	0.18
T – 30–90	8	2	27	17	4.00

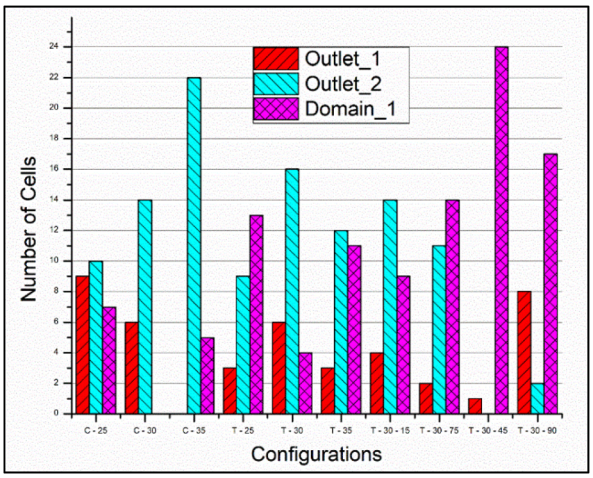

Fig. 8 The particle distribution in outlet_1, outlet_2 and the domain_1 at the end of the simulation time scale of 0.1 s as observed with triangular micropillars having pointed vertex.

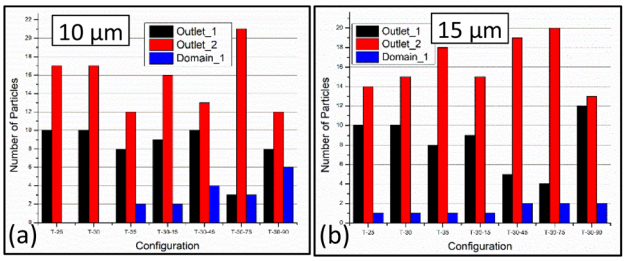

Fig. 9 The particle distribution in outlet_1, outlet_2 and the domain_1 at the end of the simulation time scale of 0.1 s observed with rounded triangular micropillars and varying particle sizes of (a) 10 µm and (b) 15 µm.

3.4 Comparison of simulations and experiments

3.4.1 Flow microscopy. Flow microscopy is conducted to observe the fluid flow pattern and the efficiency of the various DLD configurations. The setup for the flow experiments involves a fluorescence microscope (Make: Nikon, Eclipse 80i), syringe pump, BD syringes, feeder tubes, PEEK tubing and vials for collection. A food colouring dye is flown through the device to evaluate the dead zones and the fluid path in the device. The flow zone and the zero-velocity zone are seen in Fig. 11a. The zero-velocity zone is evident from the region where the cells are immobile.

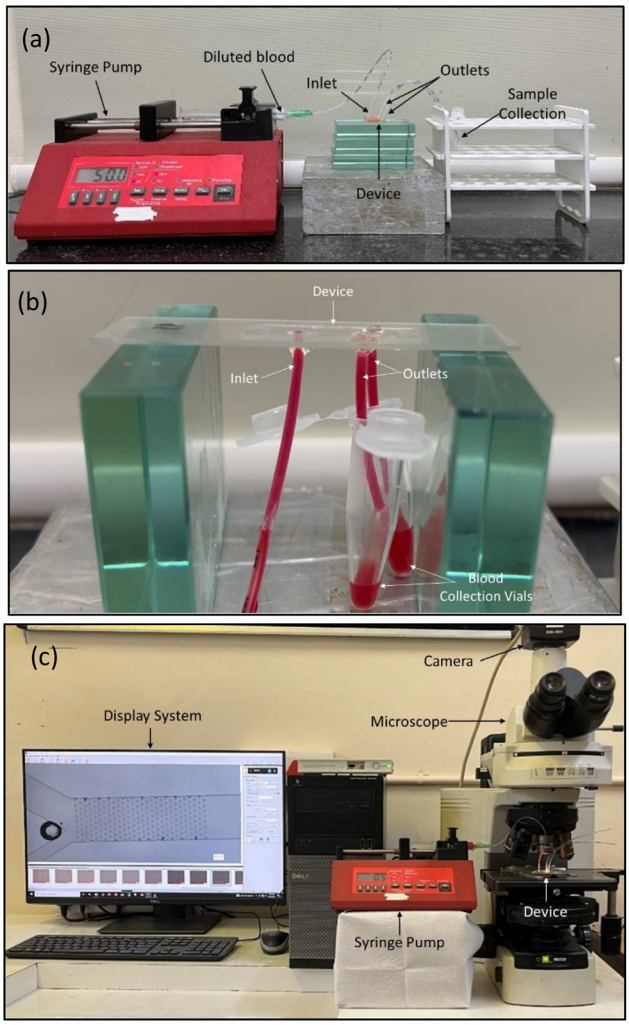

Fig. 10 Experimental setup for fluid flow and analysis. (a) and (b) Flow setup used to evaluate the cells collected at the outlets. (c) Flow setup to visualize the flow paths and the cell movement.

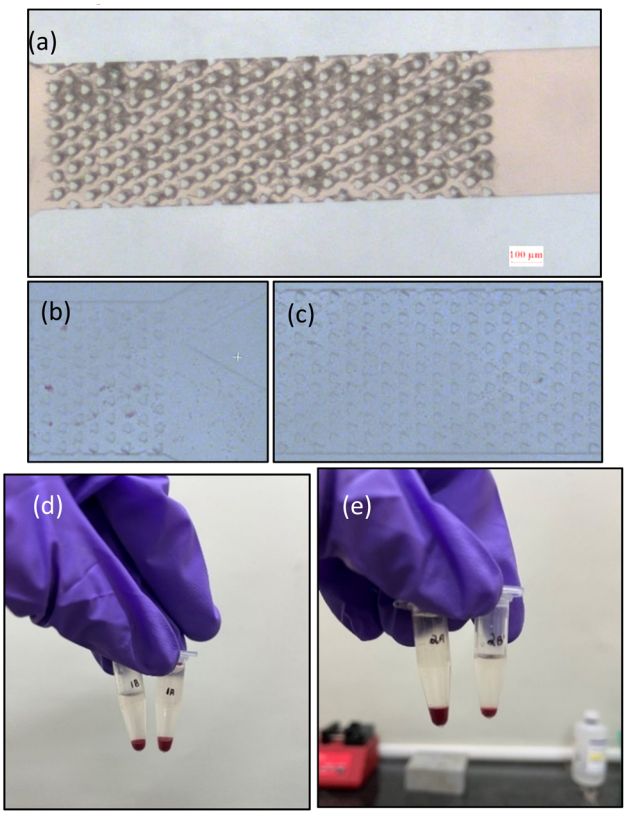

Fig. 11 (a) Food colouring dye showing the fluid path, (b) and (c) showing the flow of particles in two different sections of the device. (d) and (e) Samples collected from the outlets of the devices. "A" and "B" represents the sample collected in the left and right outlets respectively.

From the analytical measurements, the least critical particle diameter was observed to be 19.31 μm, however, lateral displacement of the blood cells (RBC – 6–8 μm and WBC – 14–16 μm) is observed in the experimental results.

Table 10 Percentage recovery in the devices corresponding to configuration

Circular micropillars			
Configuration	% recovery (%)	Configuration	% recovery (%)
C – 25	70	C – 30	74
C – 35	81		

Triangular micropillars				
Pointed vertices		Rounded vertices		
T – 25	44	T – 25	89	100
T – 30	81	T – 30	93	100
T – 35	56	T – 35	96	74
T – 30–15	67	T – 30–15	89	93
T – 30–45	4	T – 30–45	89	85
T – 30–75	48	T – 30–75	89	85
T – 30–90	37	T – 30–90	93	74

The percentage recovery in the experiments was evaluated using the eqn (10) and is tabulated in Table 10. It is found that the recovery factor varies from 44% to 81% in pointed vertex micropillars, whereas it varies from 74% to 100% in the rounded vertex micropillars.

$$\% \text{ recovery} = \frac{\text{outlet } 1 + \text{outlet } 2}{\text{inlet}} \times 100 \quad (10)$$

3.4.2 Cell counting. Cell counting is done using image processing, Fig. 12a–c show the three steps involved in cell counting. It is observed that the number of cells counted in the blood flow experiments shows a similar trend in comparison to the numerical simulation results observed in Fig. 9a and b. Fig. 13 shows the variation in the number of cells in different domains observed in the experiments. Further, Fig. 11b shows the cells adhering to the micropillars as evident in Fig. S3h† corresponding to configuration 8 (T-30–45), *i.e.*, micropillars are placed at a row shift angle of 30° and are oriented at an angle of 45°. The experimental results are found to be in agreement with the simulation results.

From the numerical simulations and the experimental studies carried out it is seen that the shape and orientation of the micropillars play an important role in evaluating the functionality of the deterministic lateral displacement-based

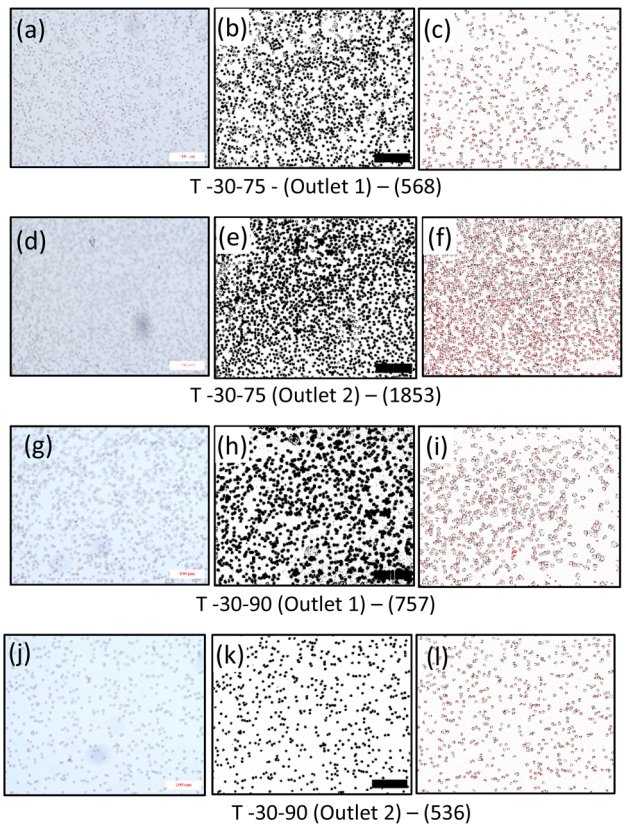

Fig. 12 (a), (d), (g) and (j) Microscope images of the cells placed on the haemocytometer, (b), (e), (h) and (k) processed images, (c), (f), (i) and (l) automated cell counting for configurations 9 (T-30–75) and 10 (T-30–90) respectively.

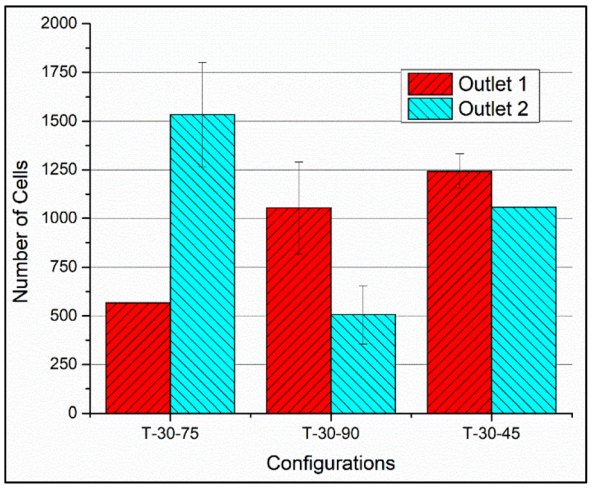

Fig. 13 The number of cells observed in outlet 1 and outlet 2 in the critical configurations.

devices. Moreover, fluid constituents can be easily manoeuvred with the triangular pillars as the pillars have faces that can be easily oriented, unlike the circular pillars. From the numerical and the experimental results is observed that the triangular micropillars with an orientation of 75° gives the best separation efficiency amidst the chosen configurations. Further, while discussing the process parameters involved in the design and fabrication of the DLD structures, it also signifies the possibility of particle separation using DLD structures at high row shift angles.

4 Discussion

From the literature, it is observed that most of the DLD-based particle separation devices are produced using SU-8 lithography and lift-off or direct writing methods, and the depth of the micropillars is restricted to 20–30 μm. However, in the current study, the depth of the microchannels and the micropillars is 95–100 μm with the diameter of the circular micropillars as 40 μm and the width of the triangular micropillars in the range of 28 μm. Thus, the fabrication is carried out using positive photoresist and DRIE Bosch process resulting in anisotropic etching to realise the required aspect ratio. The alternating deposition and etch cycles result in anisotropic etching, which is significant in the fabrication of features with a high aspect ratio. The process parameters and the DRIE cycles are crucial in defining the shape, size and quality of the structures.

From the 3D profilometer images shown in Fig. 6d and e, it is evident that the shapes of the holes also play an important role in defining the etch rate and the aspect ratio of the holes. The etching rate is higher in circular than triangular holes. And since the area of exposure on the site beside the channels is higher, the rate of etching is much higher than the micro-holes. This can be attributed to the reach of the etchant gases into the etching region. The narrower the etching region, the lower the etching depth in comparison to the wider regions.

Bond strength between the chips in the microfluidic devices depends on the plasma exposure time and the post-exposure baking temperature. Moreover, the bond strength is also considered to be critical in designing the maximum permissible pressure difference in the microfluidic chip. Thus, using the Hagen–Poiseuille equation (eqn (8)), the maximum flow rate of the fluid flowing in the chip is evaluated and shown in Table 8. Further, the maximum flow velocity is calculated using the continuity equation (eqn (9)). From the T-peel tests, the results shown in Table 7 show that the oxygen plasma bonding bond strength is 10% higher than the argon plasma with a maximum bond strength of 0.404 N mm^{-1}. It is observed that the bonding in the chips exposed to oxygen plasma for 5 min resulted in the highest bond strength in combinations carried out. This can be attributed to the formation of a large number of free sites for bonding thus increasing the availability of the bonding sites. The maximum flow rate and maximum fluid velocity achievable are 135 μL s^{-1} and 1.08 m s^{-1}. It is also observed that the hydrophilic nature of the Ar plasma exposed surface does not vanish with time, as seen in O_2 plasma bonding. As observed previously by Malecha *et al.*,[31] the surface exposed to Ar plasma showed an irreversible change in the hydrophobicity. Thus, Ar plasma is not preferred in device fabrication as it induces a small amount of hydrophilicity. This affects the functioning of the microfluidic device by inducing unwanted drag forces. This suggests the application of oxygen plasma over argon plasma. Hence, in the development of the current device, oxygen plasma is used. The flow velocity of 0.5 m s^{-1} is used for the experiments as the available volume for the flow is constricted in the DLD zone, thereby increasing the fluid pressure.

With the flow parameters and the wall conditions, the devices were tested for blood particle separation. The effect of the placement, orientation and shape of the micropillars on the particle separation was studied. It is evident from the particle tracing simulations that every configuration results in a unique flow pattern. From the results obtained in the configuration C-25, C-30 and C-35, it can be concluded that the particles are moved towards the outlet 2. However, the flow pattern in the devices with the triangular pillars is different suggesting that the shape of the pillars is significant in directing the particles. It is seen that increasing the row shift fraction in the circular DLD increases the possibility of the particles moving towards the outlet 2 whilst the triangular pillars present a completely different pattern, the number of particles reaching the outlet 2 depends on the orientation of the pillars. This can be attributed to the inter-pillar gap and the velocity profile between the pillars. As observed by Loutherback *et al.*,[22] the velocity profile of the fluid flowing between the triangular pillars is skewed in comparison to the fluid flowing between the circular pillars, thus affecting the streamlines. A similar phenomenon occurs when the orientation of the pillars is considered. The inter-pillar gap changes significantly; thus, the flow pattern obtained is skewed, and an orientation of 75° gives the best outlet 1 to outlet 2 ratio. The other important factor can be the first critical angle at the instant when the particle leaves the pillar that determines the path taken by the particles.[4]

The possibility of the particles getting stuck in the domain increases with the zero velocity zones offered to the flow on the walls of the microchannels and the walls of the pillars. The zero velocity zones are observed at the walls of the circular pillars.[29]

The recovery factor in these devices is also dependent on the configurations, it is seen that the recovery rate varied from 44% to 81%, and C-35 and T-30 result in the highest recovery factor when the pillars with the pointed vertices are considered. The recovery factors for the devices with pillars having rounded vertices were found to vary between 74% and 100%, this suggests that the rounded triangular micropillars provided a higher recovery in comparison to the pointed micropillars. The recovery factor of the configurations can be further improved using surface treatment with hydrophobic agents or other surface modification techniques.

The experiments were carried out to validate the simulations. The experimental flow study was carried out in two different ways, one keeping the device upright and the other with a reversed position, to understand the effect of gravitational forces. In the upright position, the outlets are facing upwards, and thus, there's a possibility of backward flow due to the requirement of high-pressure head. Thus, the collection tube was placed at a lower position such that the pressure head didn't affect the flow. The flow in the upright and reversed positions yields the same results. However, since the placement of the tubing in the devices is easier in the upright position, the devices in the upright position with an inverted microscope give an optimal configuration to capture the flow through the microchannels. Moreover, the strategy of collecting the samples at the outlets and enumerating the cells from the microscopic images helps reduce the error caused by visual counting using a haemocytometer.

In the manufacturing aspect, the increase in the row shift angle results in a reduction the number of pillars required for the particles to separate. The previous DLD chips consider a low inclination angle, which makes the manufacturing process difficult and also leads to the breakage of the micropillars, creating voids in the chips. In this study, an row shift angle of 25°, 30° and 35° is considered, thus reducing the pillars in the DLD zone. Increasing the inclination angle increases the inter-row and inter-column spacing, thereby increasing the number of ways the pillars can be fabricated. As observed in our previous study, laser micromachining was used to fabricate the DLD structures, but it was observed that the micro holes fused with each other when the inter-array gap was reduced to 25 μm.

Particle separation through a deterministic lateral displacement is a hydrodynamic phenomenon. Hence, it depends on the factors causing changes in the hydrodynamic forces. The laminar flow in the microchannels is affected by the roughness elements. The hydrodynamic drag and the pressure drop across the microchannels tend to change, thus aiding in particle separation. Literature suggests the application of sheath layers to avoid wall friction and considers the particle separation only between the pillars. In this study, the effect of wall friction is also considered as it is a significant factor in determining the separation efficiency of the device. Here, whole blood or diluted blood is flown through the microchannel, where the blood constituents experience the drag from the walls of the device until they reach the DLD zone and further experience deviation in the flow path due to the pillars placed in their flow direction. It is also seen that the separation efficiency depends on the first angle of incidence.

Thus, with this study, it is observed that efficient particle separation is possible even at higher row shift angles. The numerical studies can be further extended to 3 dimensional analysis to consider the friction and intercellular interactions in the particle movement. This work considers the stationary and rigid micropillars for its analysis, whereas at higher flow rates, the bending of the pillars can be observed, thus in the further studies the bending in the micropillars can be considered. The effect of the bending on the interpillar spaces, thus their effect on the particle separation can be analysed. The current work doesn't consider the effect of hydrodynamic nature of the pillars and the walls caused by the exposure to the plasma, in further studies, there is scope of introduction of these forces in determining the particle flow paths. As, the bond strength experiments show that the maximum achievable flow rates in these microfluidic devices are in the range of 100–135 μL s^{-1}, this strategy can be utilised in the development of closed microfluidic devices with higher throughput.

5 Conclusions & scope

The current study presents the life cycle of the fabrication and testing of the polymeric DLD device. The effect of the geometry, orientation and placement of the micropillars in the separation of the particles is studied. During the fabrication of the dies for devices, the effect of the process parameters during DRIE and device bonding are studied. It is observed that the etch rates vary with shapes, *i.e.*, the circular holes provide a higher depth in comparison to the triangular holes while keeping the etching parameters constant. From the bonding experiments, it is observed that the oxygen plasma provides a bond strength of 0.404 N mm^{-1}, thus a maximum flow rate of 135 μL s^{-1} is achievable. With the flow simulations and experiments, it is evident that the particle separation can be carried out at higher row shift angles, thus reducing the number of columns required to visualise the lateral displacement without compromising the resolution, thus reducing the tolerances and increasing the possible techniques with which the DLD structures can be fabricated. This also reduces the dependence on photolithography for the fabrication of these devices.

In the further studies, the simulations can be improvised for 3-dimensional study as the drag forces on the walls play a vital role in determining the number of particles getting separated. The role of the plasma exposure and the surface quality of the devices can be studied, thus providing more insights on the effect of fabrication technique on the actual particle separation. The micropillars in the current study are considered to be stationary and rigid, but at higher velocities, the micropillars are deemed to bend, and as a result, there is a variation in the interpillar gap and thus might influence the particle flow path.

Abbreviations

Ar	Argon
p	Pressure
D_c	Critical diameter
RF	Radio frequency
A_c	Cross-sectional area
Re	Reynolds number
DRIE	Deep reactive ion etching
λ	Row shift fraction
ρ	Density
SSP	Single side polished
DLD	Deterministic lateral displacement
UV	Ultraviolet
Γ	Dynamic viscosity
v	Velocity
EDTA	Edetic acid
μ	Viscosity
G	Gap size
v_x	x component for velocity
D_H	Hydraulic diameter
v_y	y component for velocity
ICP	Inductively coupled plasma
E	Young's modulus
PDMS	Polydimethylsiloxane
SU-8	Negative photoresist
PEEK	Polyether ether ketone

Author contributions

Pavan Pandit: conceptualisation, investigation, visualisation, writing – original draft. Lingxue Kong: funding, resources, supervision, writing – review & editing. GL Samuel: project administration, funding, resources, supervision, writing – review & editing.

Conflicts of interest

The research work is a part of patent application no.: 202241004133 filed on 25/01/2022 under the Indian Patents Act 1970.

Acknowledgements

This work was performed in part at the Melbourne Centre for Nanofabrication (MCN) in the Victorian Node of the Australian National Fabrication Facility (ANFF). Pavan Pandit would like to acknowledge the IITM International Immersion Experience program for facilitating the research visit to Melbourne.

References

1 J. He, M. Huang, D. Wang, Z. Zhang and G. Li, *J. Pharm. Biomed. Anal.*, 2014, **101**, 84–101.
2 M. Hejazian, W. Li and N. T. Nguyen, *Lab Chip*, 2015, **15**, 959–970.
3 N. Pamme, *Curr. Opin. Chem. Biol.*, 2012, **16**, 436–443.
4 T. Bowman, J. Frechette and G. Drazer, *Lab Chip*, 2012, **12**, 2903–2908.
5 H. N. Joensson, M. Uhlén and H. A. Svahn, *Lab Chip*, 2011, **11**, 1305–1310.
6 A. Kühnlein, Master's thesis, Lund University, 2016.
7 L. R. Huang, E. C. Cox, R. H. Austin and J. C. Sturm, *Science*, 2004, **304**, 987–990.
8 W. Su, H. Li, W. Chen and J. Qin, *TrAC, Trends Anal. Chem.*, 2019, **118**, 686–698.
9 B. H. Wunsch, J. T. Smith, S. M. Gifford, C. Wang, M. Brink, R. L. Bruce, R. H. Austin, G. Stolovitzky and Y. Astier, *Nat. Nanotechnol.*, 2016, **11**, 936–940.
10 J. A. Davis, D. W. Inglis, K. J. Morton, D. A. Lawrence, L. R. Huang, S. Y. Chou, J. C. Sturm and R. H. Austin, *Proc. Natl. Acad. Sci. U.S.A.*, 2006, **103**, 14779–14784.
11 N. Li, D. T. Kamei and C.-M. Ho, in *2007 2nd IEEE International Conference on Nano/Micro Engineered and Molecular Systems*, 2007, pp. 932–936.
12 S. Ranjan, K. K. Zeming, R. Jureen, D. Fisher and Y. Zhang, *Lab Chip*, 2014, **14**, 4250–4262.
13 S. Zheng, R. Yung, Y.-C. Tai and H. Kasdan, in *18th IEEE International Conference on Micro Electro Mechanical Systems, 2005, MEMS 2005*, 2005, pp. 851–854.
14 J. A. Davis, Microfluidic Separation of Blood Components through Deterministic Lateral Displacement, PhD Thesis, Faculty of Princeton University, 2008.
15 Z. Liu, F. Huang, J. Du, W. Shu, H. Feng, X. Xu and Y. Chen, *Biomicrofluidics*, 2013, **7**, 011801.
16 Z. Liu, Y. Huang, W. Liang, J. Bai, H. Feng, Z. Fang, G. Tian, Y. Zhu, H. Zhang, Y. Wang, A. Liu and Y. Chen, *Lab Chip*, 2021, **21**, 2881–2891.
17 D. W. Inglis, J. A. Davis, R. H. Austin and J. C. Sturm, *Lab Chip*, 2006, **6**, 655–658.
18 B. M. Dincau, A. Aghilinejad, X. Chen, S. Y. Moon and J. H. Kim, *Microfluid. Nanofluid.*, 2018, **22**, 137.
19 S. H. Holm, J. P. Beech, M. P. Barrett and J. O. Tegenfeldt, *Lab Chip*, 2011, **11**, 1326–1332.
20 K. K. Zeming, S. Ranjan and Y. Zhang, *Nat. Commun.*, 2013, **4**, 1625.
21 K. Loutherback, J. Puchalla, R. H. Austin and J. C. Sturm, *Phys. Rev. Lett.*, 2009, **102**, 045301.
22 K. Loutherback, K. S. Chou, J. Newman, J. Puchalla, R. H. Austin and J. C. Sturm, *Microfluid. Nanofluid.*, 2010, **9**, 1143–1149.
23 J. Wei, H. Song, Z. Shen, Y. He, X. Xu, Y. Zhang and B. N. Li, *IEEE Trans. NanoBiosci.*, 2015, **14**, 660–667.
24 E. Pariset, C. Pudda, F. Boizot, N. Verplanck, J. Berthier, A. Thuaire and V. Agache, *Small*, 2017, **13**, 1701901.
25 Z. Zhang, E. Henry, G. Gompper and D. A. Fedosov, *J. Chem. Phys.*, 2015, **143**, 243145.
26 K. Patel and H. Stark, *Soft Matter*, 2021, **17**, 4804–4817.
27 D. W. Inglis, M. Lord and R. E. Nordon, *J. Micromech. Microeng.*, 2011, **21**, 054024.
28 S. Motahhari and J. Cameron, *J. Reinf. Plast. Compos.*, 1999, **18**, 1011–1020.
29 P. Pandit and G. L. Samuel, *Appl. Phys. A: Mater. Sci. Process.*, 2022, **128**, 878.

30 C. F. Chen and K. Wharton, *RSC Adv.*, 2017, **7**, 1286–1289.
31 K. Malecha, I. Gancarz and W. Tylus, *J. Micromech. Microeng.*, 2010, **20**, 115006.
32 M. P. Manning, D. Sc thesis, Massachusetts Institute of Technology, 1976.
33 D. G. Merck KGaA, *Technical Datasheet AZ 40XT-11D Photoresist*.
34 K. S. Chen, A. A. Ayón, X. Zhang and S. M. Spearing, *J. Microelectromech. Syst.*, 2002, **11**, 264–275.
35 B. Rezaei, M. Moghimi Zand and R. Javidi, *J. Chromatogr. A*, 2021, **1649**, 462216.